Research article

Synthesis of Flower-like Kesterite Cu_2ZnSnS_4 Nanostructures using Different Sulfur Sources and Applications

Manjula Selvam[1], Sarathkumar Anbuselvan[1], Nithish Kumar Srinivasan[1], Mohanraj Kannusamy[2], HO Soon min[3] and Sivakumar Ganesan[1]*

[1]*Department of Physics, Annamalai University, Annamalai Nagar, Tamil Nadu, India*
[2]*Department of Physics, School of Basic and Applied Sciences, Central University of Tamil Nadu, Thiruvarur - 610 101, India*
[3]*Faculty of Health and Life Science, INTI International University, Putra Nilai 71800, Malaysia*

Curr. Appl. Sci. Technol. 2024, Vol. 24 (No. 6), e0260708; https://doi.org/10.55003/cast.2023.260708

Received: 27 September 2023, Revised: 8 January 2024, Accepted: 10 June 2024, Published: 16 August 2024

Keywords

surfactant-free;
hydrothermal;
kesterite CZTS;
flower-like;
specific capacitance;
antibacterial activity

Abstract

In this study, surfactant-free quaternary copper zinc tin sulfide (CZTS) nanostructures were successfully synthesized using two different chalcogen/sulfur precursors by hydrothermal method. The effects of different sulfur sources such as thiourea (TU) and thioacetamide (TAA) on the structural, functional, and morphological properties were investigated. XRD analysis revealed that pure phase of kesterite CZTS nanostructures were found at higher concentrations of thiourea. Raman studies proved the existence of the phase purity of CZTS at TU-10. Morphological investigation of CZTS nanostructures showed different morphologies such as spherical-like, rose flower-like, and plate-like structures, at different concentrations of thiourea. Structural and morphological studies confirmed that the formation of single-phase CZTS nanostructures was possible at higher concentrations of TU. HRTEM analysis of CZTS TU-10 confirmed that the lattice value of 0.31 nm corresponded to the (112) plane and the SAED pattern exhibited a polycrystalline nature. EDS mapping of CZTS nanostructures confirmed its uniform distribution. The optical bandgap of CZTS TU-10 was found to be 1.52 eV. XPS results revealed Cu^{2+}, Zn^{2+}, Sn^{4+}, and S^{2-} oxidation states for CZTS TU-10. Cyclic voltammetry of CZTS TU-10 showed the pseudocapacitive nature and the specific capacitance of 389 Fg^{-1} at 10 mV/s. Furthermore, the photocatalytic activity of the surfactant-free CZTS TU-10 nanostructures was tested using methylene blue (MB) and crystal violet (CV) degradation under visible light irradiation, and

*Corresponding author: E-mail: gsk.csil@gmail.com

the maximum photodegradation efficiencies achieved were at 89% and 93%, respectively, at 70 min. Furthermore, antibacterial studies confirmed that CZTS TU-10 nanostructures produced a high zone of inhibition against *Vibrio parahaemolyticus*. The results implied that the CZTS nanostructures could be considered efficient for energy storage and photocatalytic application.

1. Introduction

Due to rising global pollution, sustainable renewable resources have captured global attention and accelerated the development of environmentally friendly energy sources. Because energy harvesting from renewable energy sources is so prevalent today, research is also focused on various strategies for storing this energy in the form of electricity. Alternative fuels and energy storage technologies such as improved batteries, fuel cells, ultracapacitors including assessments present a significant challenge to the use of petroleum-based fuels [1-3]. Electrochemical supercapacitors are gaining much attention among the various energy storage technologies because of their exceptional durability, elevated energy and power density, expedited redox processes for charging and discharging, environmentally sustainable attributes, and cost-effectiveness [4-6]. Supercapacitors are categorized into two types based on their energy storage mechanisms: electric double-layer capacitors (EDLCs) and pseudo capacitors. Supercapacitors or ultracapacitors, commonly referred to as EDLCs, are energy storage devices with a higher energy density than batteries and a higher power density than conventional capacitors. Pseudo capacitors, alternatively referred to as faradaic supercapacitors, are different to EDLCs in that their capacitance arises from reversible and rapid faradaic processes (redox processes) occurring in close proximity to the electrode surface [7]. Generally, hydroxides, metal oxides, polymers, and nitrogen sulfides are widely used in pseudocapacitive materials. Metal oxides are commonly chosen as the preferred materials for exhibiting pseudocapacitive behavior [8]. However, the restricted dielectric potential between the electrode and the electrolyte prevents effective electron movement. To address this issue, metal sulfides which are more structurally stable than oxides have been used due to sulfur having a lower electronegativity than oxygen, which enables rapid electron transport [9, 10]. Quaternary metal chalcogenides are formed when different metals are combined with at least one chalcogen element, such as sulfur, selenium, or tellurium [11]. Among the quaternary chalcogenides (Cu_2NiSnS_4, Cu_2ZnSnS_4, and Cu_2MnSnS_4), copper zinc tin sulfide (Cu_2ZnSnS_4) is currently a promising material since the components are nontoxic, earth-abundant, and of low cost, have a high absorption coefficient and are eco-friendly [12]. Copper zinc tin sulfide (CZTS) exists in three different crystal forms: kesterite (I), stannite (I 2 m), and wurtzite (P63mc). The most stable of the three structures is the kesterite phase of CZTS, which is generated from the copper indium gallium selenide (CIGS) structure by the isoelectronic substitution of zinc and tin for indium and gallium, respectively [13]. Additionally, CZTS is a p-type semiconducting material with a wide range of thermoelectric, photocatalytic, and energy harvesting applications [14]. Although CZTS nanoparticle synthesis has been highly reported, there are still some significant problems with the materials. The formation of this compound is complicated by the multiple components that go into its production. Due to the intrinsically small composition zone for single-phase CZTS, the simplicity of component vaporization, and the high chemical potential for secondary phase formation, the formation of a pure single-phased structure of this product without additives is extremely difficult [15-17]. Yu *et al*. [18] reported the controlled synthesis of pure-phase CZTS nanocrystals using an oleyl amine (OLA) surfactant. Polyvinyl pyrrolidone (PVP) surfactant was used in the synthesis of copper iron tin sulfide by solvothermal method. Additives such as surfactants, binding agents, or capping agents are a significant drawback in the synthesis of nanoparticles [19] owing to the need to remove the additive from the sample after nanoparticle formation. Also, when surfactants are used in large

quantities in the industry, they cause harmful environmental pollution [20]. Therefore, the surfactant-free syntheses of nanoparticles are currently being encouraged. From the literature data, it was noticed that there was a paucity of results on synthesizing single-phase CZTS with a surfactant-free manner [21]. Zaman *et al*. [22] and Chaudhari *et al*. [23] reported on the photocatalytic, antibacterial, and electrochemical properties of the prepared CZTS nanostructures and their applications.

The novelty of the present work is to synthesize template-free (i.e. surfactant/binding/structural agents) Cu_2ZnSnS_4 nanoparticles by the hydrothermal method with various sulfur sources (thiourea and thioacetamide) at different concentrations. Furthermore, the major objective is to assess how different sulfur sources and their concentrations influence the synthesis of single-phase CZTS nanostructures. This study also explores the specific capacitance of CZTS nanostructures through cyclic voltammetry (CV) and galvanostatic charge-discharge (GCD) techniques. The photocatalytic activity of CZTS nanoparticles was investigated for their ability to degrade environmentally harmful dyes like crystal violet (CV) and methylene blue (MB), under solar radiation. In addition, the antibacterial activity of CZTS nanostructures was examined against gram-positive and gram-negative bacteria by agar well diffusion method.

2. Materials and Methods

Copper chloride dihydrate ($CuCl2{\cdot}2H2O$ > 99.5% purity), zinc nitrate hexahydrate ($Zn(NO_3)_2{\cdot}6H_2O$ > 98.0% purity) and stannous chloride dihydrate ($SnCl_2{\cdot}2H_2O$ > 99.5% purity) were used as the metal precursors of Cu, Zn, and Sn, respectively. For sulfur sources, thioacetamide (TAA) (C_2H_5NS > 97.0% purity) and thiourea (TU) ($NH_2{\cdot}CSNH_2$ > 99.5% purity) were used. All the compounds were acquired from Sigma-Aldrich at AR grade and used without purification.

The crystal structure and phase formation of the synthesized nanoparticles were confirmed through the powder X-ray diffractometer (X'pert PRO – Panalytic, Netherlands) with Cu Kα radiation (λ = 1.54060Å), and the Micro-laser Raman spectrometer (Seiki, Japan), respectively, available at Alagappa University, Karaikudi, India. Field emission scanning electron microscopic (FESEM) images of the CZTS nanoparticles were obtained using Germany Carl Zeiss –Sigma-300 equipped with EDAX available at Annamalai University, Tamil Nādu, India. The structural properties of CZTS nanoparticles were further characterized by a transmission electron microscopy (TEM, Tecnai G^2 20 S-Twin, Japan) with a voltage of 200 kV, available at Madurai Kamaraj University, Madurai. A PHI-VERSAPROBE III X-ray photoelectron spectroscopy technique (XPS) was used to examine the surface chemical state and composition of the CZTS. The optical band gap of the material was examined using a Thermo Fisher Evolution (220 UV-DRS, USA) spectrophotometer. A UV–Vis spectrophotometer (UV-1800, Shimadzu, Japan), available at Annamalai University, Tamil Nadu, was used to investigate the photocatalytic degradation of dyes.

2.1 Synthesis of Cu_2ZnSnS_4 (CZTS) nanostructures

CZTS nanostructures were synthesized by the hydrothermal method using thiourea (TU) as a sulfur source. The molar ratio [Cu:2, Zn:1, Sn:1, Tu:4 (TU-4)] of CZTS nanostructures was prepared as follows: 0.08 M copper chloride dihydrate (0.136 g/10 mL), 0.04 M zinc nitrate hexahydrate (0.059 g/5 mL), 0.04 M stannous chloride dihydrate (0.045 g/5 mL), and 0.16 M thiourea (TU - 0.243 g/20 mL) were separately dissolved in double distilled water. Each solution was stirred for 30 min, transferred into a teflon-lined stainless-steel autoclave, and kept in a muffle furnace for 24 h at 210°C. After the reaction was finished, the autoclave was allowed to cool naturally to room temperature. The obtained precipitate was cleaned using distilled water and ethanol and then dried

for 3 h in a hot air oven at 70°C. To examine the impact of different sulfur concentrations on the structural, morphological, and functional group features of CZTS nanostructures, the above procedure was used to synthesize TU-6 (2:1:1:6), TU-8 (2:1:1:8), and TU-10 (2:1:1:10) samples. In addition, the same synthesis procedure was used to prepare CZTS nanostructures using thioacetamide (TAA) instead of TU. The prepared samples were named TAA-4 (2:1:1:4), TAA-6 (2:1:1:6), TAA-8 (2:1:1:8), and TAA-10 (2:1:1:10).

2.2 Photocatalytic measurements

The degradation of methylene blue (MB) and crystal violet (CV) dyes in aqueous solution using a UV-Vis spectrophotometer was used to measure the photocatalytic reaction of CZTS (TU-10) nanostructures. Initially, 0.05 g of prepared CZTS nanoparticles was added to 100 mL of a blank solution containing 10^{-4} mol/L CZTS. To achieve adsorption-desorption equilibrium between the catalyst and dye, a beaker containing the dye solution and the catalyst (CZTS) was left in dark conditions for 30 min. The pH of the MB and CV dye solutions was ~6 during the photocatalytic activity. The photocatalyst was illuminated with solar light. All photocatalytic experiments were conducted during April, from 11 a.m. to 2 p.m., on bright sunny days with continuous stirring achieved with a magnetic stirrer on the top roof of the building.

The photocatalytic degradation efficiency was evaluated by equation (1),

$$\text{Efficiency } (\eta\%) = \left(1 - \frac{C}{C_o}\right) \times 100 \quad (1)$$

where C_o and C are the initial and variable absorbance of the dye, respectively.

2.3 Preparation of the CZTS electrode

The CZTS TU-10 electrode was prepared using a nickel plate previously polished with sandpaper and ultrasonicated in ethanol for 60 min. A slurry paste containing 80 wt.% CZTS powder, 10 wt.% polyvinylidene difluoride, and 10 wt.% carbon black can be formed by dropwise addition of the needed amounts of N-methyl pyrrolidone (NMP). The prepared paste was applied to a nickel plate with an active area of 1 cm×1 cm and dried at 120°C overnight. The weight of the active mass materials in the working electrode was 5 mg. In the three-electrode system, the prepared CZTS was used as the working electrode, platinum wire was the counter electrode and Ag/AgCl was used as the reference electrode.

2.4 Electrochemical performance of the supercapacitor

The specific capacitance of the CZTS electrode was calculated by cyclic voltammetry measurements in the range of a potential window of 0 to 0.6 mV/s with varying scan rates. Additionally, galvanostatic charge-discharge analysis was performed at different current densities with a potential window ranging from 0 to 0.6 V. To determine the specific capacitance (C_{sp}) of the CZTS electrode the following equations were evaluated [24].

For cyclic voltammetry,

$$C_{sp} = \frac{\int I\Delta t}{Sm\Delta v} \text{ F/g} \quad (2)$$

For GCD,

$$C_{sp} = \frac{Idt}{mdV} \text{ F/g} \quad (3)$$

where 'C_{sp}' is the specific capacitance, $\int I \Delta t$ is the area of the CV curve, 's' is the scan rate (mV/s), ΔV is the potential window (V), 'm' is the mass of the loaded material (g), 'I' is the current density (A), 'dt' is the discharge time (s), and 'dV' is the potential (V).

3. Results and Discussion

3.1 Structural analysis

The XRD patterns of CZTS nanostructures using different concentrations of TU and TAA samples are shown in Figures 1(a-d) and 2(a-d), respectively. From Figure 1(a), TU-4, the sharp diffraction peaks that appear at 29.07°, 31.53°, and 32.56° can be attributed to the (102), (103), and (006) hkl planes of CuS phase, respectively (JCPDS card no – 78-2121) [25, 26]. The presence of peaks at 2θ = 47.53° and 59.12° correspond to the (220) and (224) planes, respectively, confirming the presence of tetragonal structured CZTS phase with space groups of I42m (JCPDS card no – 26-0575) [27]. By increasing the TU concentration to TU-6 (Figure 1b), and TU-8 (Figure 1c), the intensity of the characteristic peaks of CZTS, 2θ = 28.49°, 47.27°, 56.66°, and 59.31°, corresponding to the (112), (220), (312) and (224) planes, respectively, get increased. It is interesting to note that the plane corresponding to (102), (103), (006), and (108) of CuS decreases gradually. However, at higher concentrations of thiourea TU-10 (Figure 1d), the peaks corresponding to the CuS phase diminish completely and the significant peaks of CZTS at 2θ = 28.35°, 47.30°, 56.14°, and 59.26° have preferential growth along (112), (220), (312) and (224) planes, which shows the presence of CZTS alone. This finding confirmed that a higher concentration (TU-10) of sulfur is necessary to produce the single-phase kesterite CZTS phase [28]. This is because sulfur evaporates easily at high temperatures in a hydrothermal reaction [29].

The XRD patterns of the CZTS using TAA showed similar results for TAA-4 to TAA-8 as TU-4 to TU-8 as that of CZTS synthesized using TU (Figure 2(a-c)). However, at higher concentrations (TAA-10), the characteristic peaks of CZTS (28.42°, 47.88°, 56.28°, and 59.26°) appeared with additional crystalline peaks at 2θ = 31.65° and 32.72° corresponding to CuS, still showed preferential growth along the directions of (103) and (006), respectively, which was evidence of mixed phase (CuS) of CZTS nanoparticles synthesized with a higher concentration of TAA. The results were in agreement with earlier reports by Yang *et al*. [30] who observed the presence of a minor quantity of the CuS phase with CZTS. Moreover, Figure 2(d) shows the wide intense diffraction peaks of CZTS, and low-intensity secondary peaks are found at higher concentrations of TAA-10. By comparing the XRD patterns of two different sulfur sources and different concentrations, CZTS prepared at TU-10 concentration was of a single phase with better crystallinity and strong diffraction peaks. Because different metals react differently with sulfur, the type of sulfur precursor used affected the final product's structure: a faster reaction produced mixed phases, while a slower reaction produced a single phase [31].

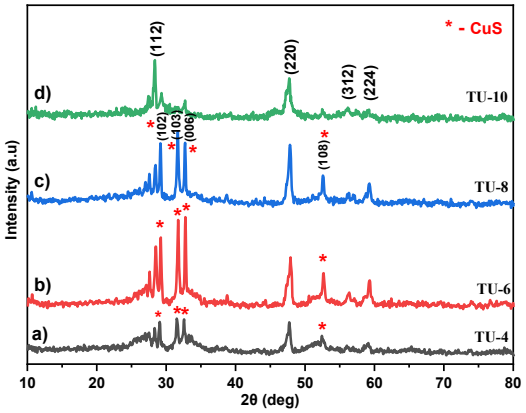

Figure 1. XRD patterns of CZTS nanoparticles at different concentrations of TU

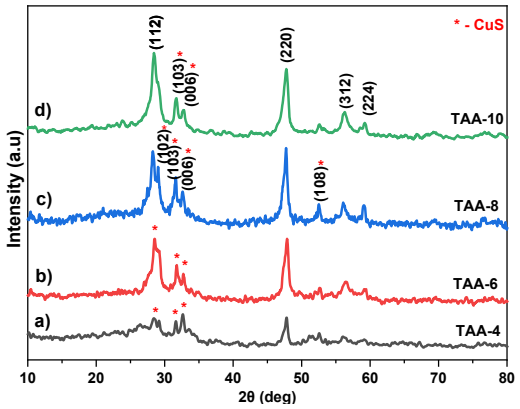

Figure 2. XRD patterns of CZTS nanoparticles at different concentrations of TAA

The crystallite size (D), dislocation density (δ), microstrain (Ɛ) and lattice parameters of the TU-10 and TAA-10 samples were calculated using the following formulae [32]:

$$D = \frac{k\lambda}{\beta cos\theta} \quad (4)$$

$$\delta = \frac{1}{D^2} \quad (5)$$

$$\varepsilon = \frac{\beta cos\theta}{4} \quad (6)$$

$$\frac{1}{d^2} = \frac{h^2 + k^2}{a^2} + \frac{l^2}{c^2} \quad (7)$$

The standard and experimental X-ray diffraction parameters were compared, as shown

in Table 1, revealing that the observed values were well-matched with standard values. The estimated crystallite size values were 38 and 28 nm for CZTS TAA-10 and TU-10 samples, respectively. The observed small crystallite sizes indicated that the synthesized CZTS samples were nanocrystalline in nature. During the hydrolysis, S^{2-} ions are gradually released due to the hydrothermal treatment decompositions of thiourea and gradually combine with cations ions to form quaternary nuclei. Accordingly, the nuclei begin to grow crystallites, undergoing preferentially oriented growth along the (112) direction when S^{2-} (TU source) is released slowly after nucleation compared to TAA [33]. Hence, the thiourea sulfur precursor had a noticeable effect on crystallite size, morphology, and single-phase CZTS formation. From Table 2, the decreased dislocation density and microstrain values due to the higher sulfur concentrations allowed material growth with the pure phase of CZTS. The lattice values were found in the range between 5.426-5.431 and 10.842-10.853 Å for samples CZTS TU-10 and TAA-10, respectively, and agreed well with standard JCPDS values. Additionally, the slight variations observed in the lattice parameters could be attributed to the different morphologies of the samples with different sulfur sources.

Table 1. X-ray diffraction parameters for CZTS at TU-10 and TAA-10 nanoparticles

Standard value (JCPDS no. 26-0575) Kesterite phase			**Observed value TU10 - 2:1:1:10 (Cu:Zn: Sn:S)**			**Observed value TAA10 - 2:1:1:10 (Cu:Zn: Sn:S)**		
2theta (deg)	**d-spacing**	**hkl**	**2theta (deg)**	**d-spacing**	**FWHM**	**2theta (deg)**	**d-spacing**	**FWHM**
28.530	3.126	1 1 2	28.354	3.147	0.147	28.423	3.140	0.246
-	-	-	-	-	-	31.652	3.063	0.147
-	-	-	-	-	-	32.727	2.736	0.196
47.329	1.919	2 2 0	47.309	1.984	0.295	47.882	1.899	0.246
56.175	1.636	3 1 2	56.142	1.638	0.590	56.285	1.634	0.492
58.967	1.565	2 2 4	58.263	1.532	0.295	59.261	1.559	0.295

Table 2. Experimental values D, δ, Ɛ and lattice constants for TU-10 and TAA-10 CZTS nanoparticles

S. No	**Sample**	**Crystallite size D (nm)**	**Dislocation density (δ)x 10^{14}(line m^{-2})**	**Micro strain (Ɛ) (10^{-3})**	**Lattice constants a=b≠c**
1	TU -10	28	12.755	0.229	a=b 5.426 c=10.842
2	TAA - 10	38	6.925	0.325	a=b 5.431 c=10.853

3.2. Raman analysis

X-ray diffraction analysis, which is commonly used for phase identification, could not be used to identify some of these phases from the stannite/kesterite CZTS, requiring the use of a complementary technique. Raman scattering analysis was helpful in the differentiation of the phases not only laterally but also in depth. The Raman spectra of CZTS nanostructures with different concentrations of TU and TAA are shown in Figures 3(a-d) and 4(a-d), respectively.

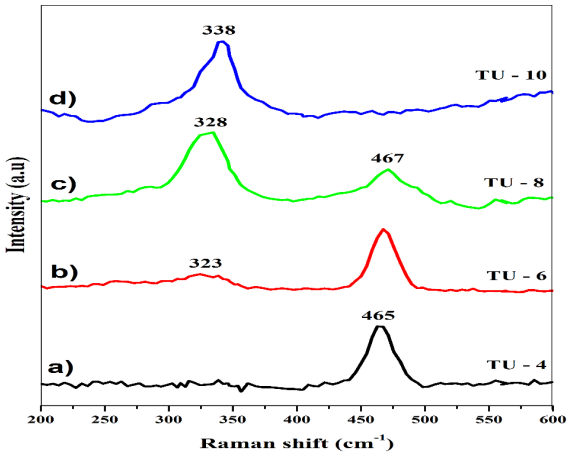

Figure 3. Raman spectra of CZTS with different TU concentrations

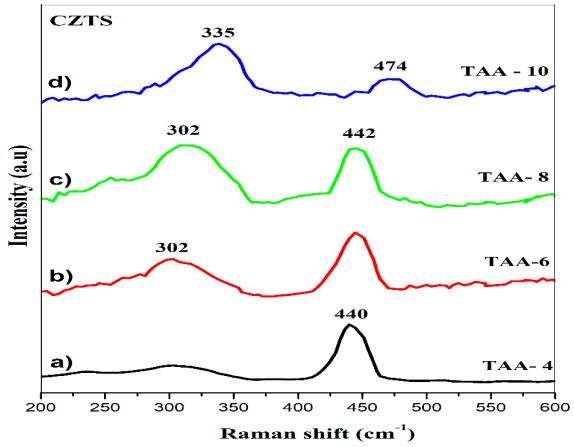

Figure 4. Raman spectra of CZTS with different TAA concentrations

In the Raman spectra of the lower concentration samples (TU-4 and TAA-4, Figures 3a and 4a), the strong Raman peak observed in the range of 440-465 cm^{-1} was due to the presence of CuS phase [34]. It could be attributed to the initial formation of copper sulfide, which acts as a catalyst for CZTS growth [35]. When TU and TAA concentrations were increased to TU-6 and TAA-6, the Raman spectra exhibited characteristic peaks at 323 cm^{-1} and 302 cm^{-1}, attributable to the CZTS phase [36]. Both the CZTS samples (Figures 3b and 4b) displayed two highly intense peaks in the region of 300-338 cm^{-1} and 440-485 cm^{-1}, which corresponded to the characteristic peak of CZTS and the secondary peak CuS respectively. Shalabayev *et al.* [37] reported a similar type of result and stated that kesterite CZTS showed a Raman peak at 338 cm^{-1}. It was noticed that the intensity of the kesterite peak (CZTS) increased with increasing sulfur concentration (TU-8 and TAA-8 (Figures 3c and 4c)).

Further, with increase of the thiourea concentration (TU-10), the mixed phase (CuS) (467 cm^{-1}) vanished as it was transformed into a single-phase CZTS (Figure 3d). The visible increase in intensity of the peak at 338 cm^{-1} corresponded to gradual increase in CZTS concentration. In the case of TAA-10, peaks appeared at 474 cm^{-1} and 335 cm^{-1} (Figure 4d), confirming that the sample TAA-10 consisted in a mixed phase of CuS and CZTS, respectively [38]. These results confirmed that the synthesized CZTS TU-10 nanostructures were pure kesterite CZTS. At lower concentrations of sulfur, the TU and TAA samples exhibited poor and mixed phases of CZTS nanostructures. Moreover, the pure phase CZTS nanostructures obtained at higher thiourea concentrations (TU-10) were confirmed through XRD patterns and Raman spectra.

3.3. Morphology analysis

The morphological features of the CZTS nanostructures produced using different chalcogen precursors were investigated by FESEM analysis. The FESEM images of CZTS samples using TAA concentrations are shown in Figure 5(a-d). At lower concentrations of TAA (4, 6), the samples showed cubic structures with an average size of approximately 50-80 nm, whereas with a higher concentration of TAA, hexagonal plate-like structures were found. The average size of a hexagonal plate was 80-100 nm. Due to the strong coupling between the $-NH_2$ group and the nanoparticles, the rate of S^{2-} release was slower when thiourea was used as the sulfur source as opposed to when other sulfur sources were used [39, 40]. Figure 6(a-d) shows FESEM images of the CZTS samples using different concentrations of TU. The lower concentration of the TU-4 samples showed irregular structures, whereas TU-6 showed spherical-like structures with plates that had a thickness of approximately 50-60 nm. Upon further increase of concentration (> TU-8), the plate-like structures transformed into nanosheets present in bundle-like formations. Finally, at the higher concentration of TU-10, the connected nanosheets formed a hierarchical rose flower-like morphology with an average size of approximately 3-5 µm (Figure 6(d). By using TU concentrations, the self-assembled CZTS flower-like nanostructures could be formed in the following steps: CZTS nanoparticles (1D) were initially prepared through homogeneous nucleation, and the growth process was followed by the formation of CZTS nanosheets (2D) owing to oriented aggregation. These CZTS TU-10 nanosheets became attached close to each other to form rose flower-like structures (3D) by the Ostwald ripening process. The flower-like structures had a large surface area and aspect ratio, and their internal parts may not be fully utilized, which was helpful in enhancing their electrochemical properties [41]. Based on this study, the size, morphological changes, nucleation extent, and structure of the synthesized CZTS nanostructures were significantly influenced by the sulfur sources. Furthermore, a unique rose-like morphology of the CZTS TU-10 sample was optimized for further characterization and application studies.

The EDS mapping of TAA-10 and TU-10 CZTS nanostructures are displayed in Figures 5e and 6e. The EDS mapping of both samples revealed the uniform distribution spots and confirmed to finding of the elements of Cu, Zn, Sn, and S, respectively. Also, EDS mapping illustrated that no other impurity spots were observed in the spectra and suggested that the prepared CZTS nanostructures were pure Cu_2ZnSnS_4 phase.

3.4 Transmission electron microscopy

To further investigate the CZTS TU-10 sample morphology and size, high-resolution transmission electron microscopy (HRTEM) was used. The different magnifications of the TEM images of the CZTS TU-10 nanostructures are depicted in Figure 7(a-b) and reveal that the nanoparticles were well dispersed with a rose flower-like structure. The average size of the flower-like structures was approximately 200 nm. Figure 7c shows a clear lattice fringe value of 0.31 nm corresponding to the

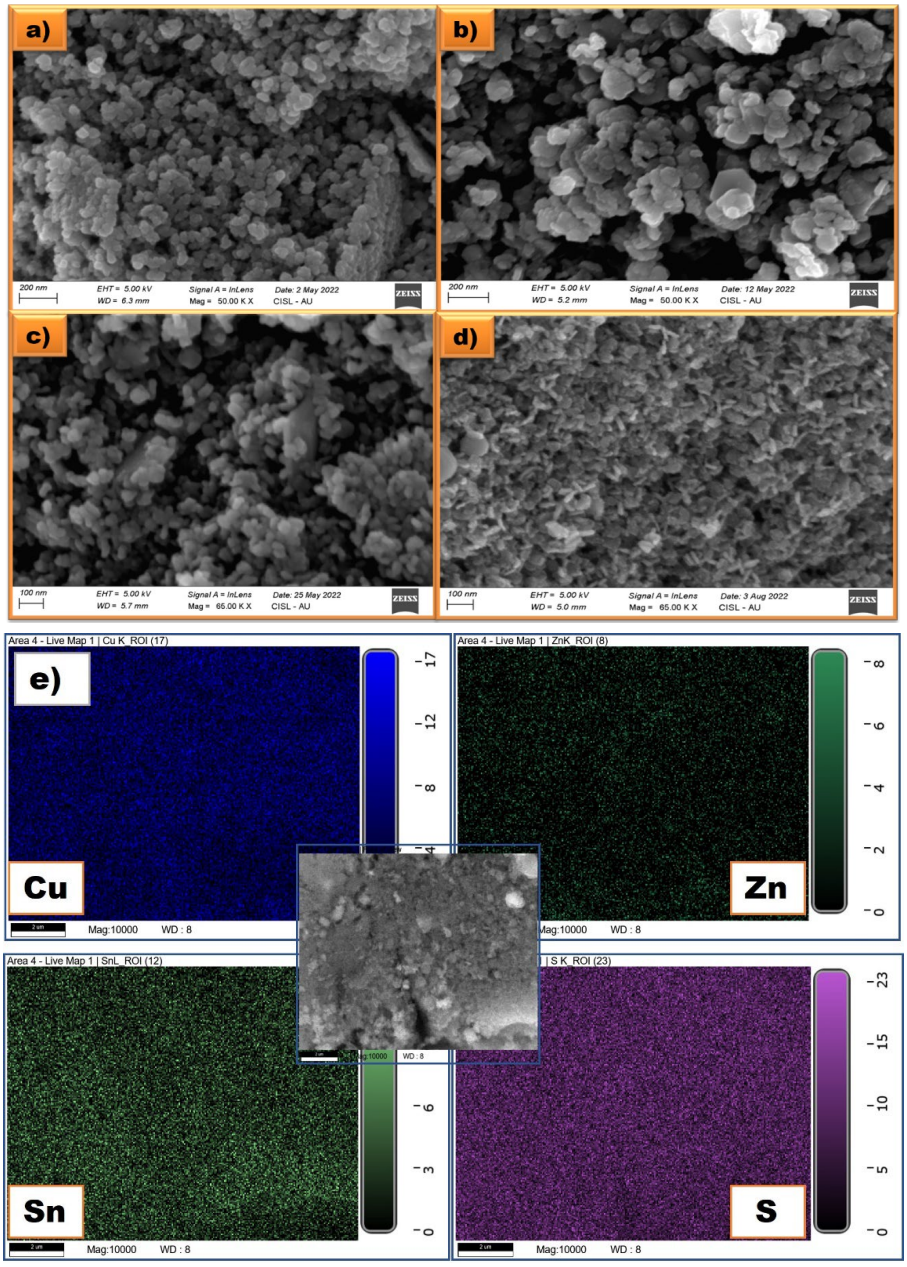

Figure 5. FESEM images of CZTS nanostructures using thioacetamide a) TAA-4, b) TAA-6, c) TAA-8, d) TAA-10 and e) Elemental mapping of CZTS nanostructures using TAA-10 sample

(112) plane of CZTS [42]. The bright spot rings in the SAED (Figure 7d) pattern were consistent with the planes observed by XRD. The presence of four diffraction rings indicates that the nanoparticles were well crystallized.

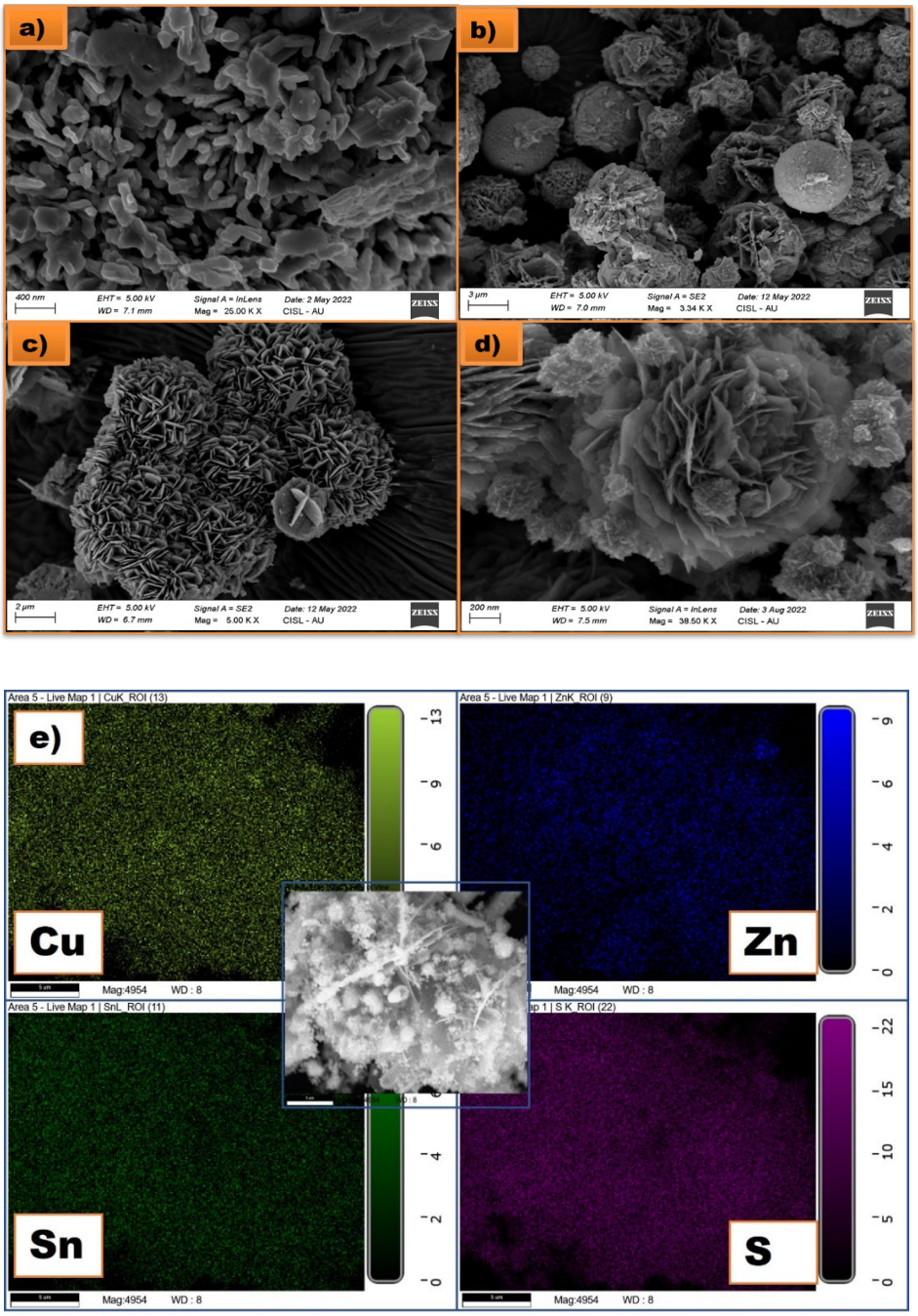

Figure 6. FESEM images of CZTS nanostructures using thiourea source a) TU4, b) TU6, c) TU8, d) TU10, and e) elemental mapping of CZTS nanostructures using TU-10 sample

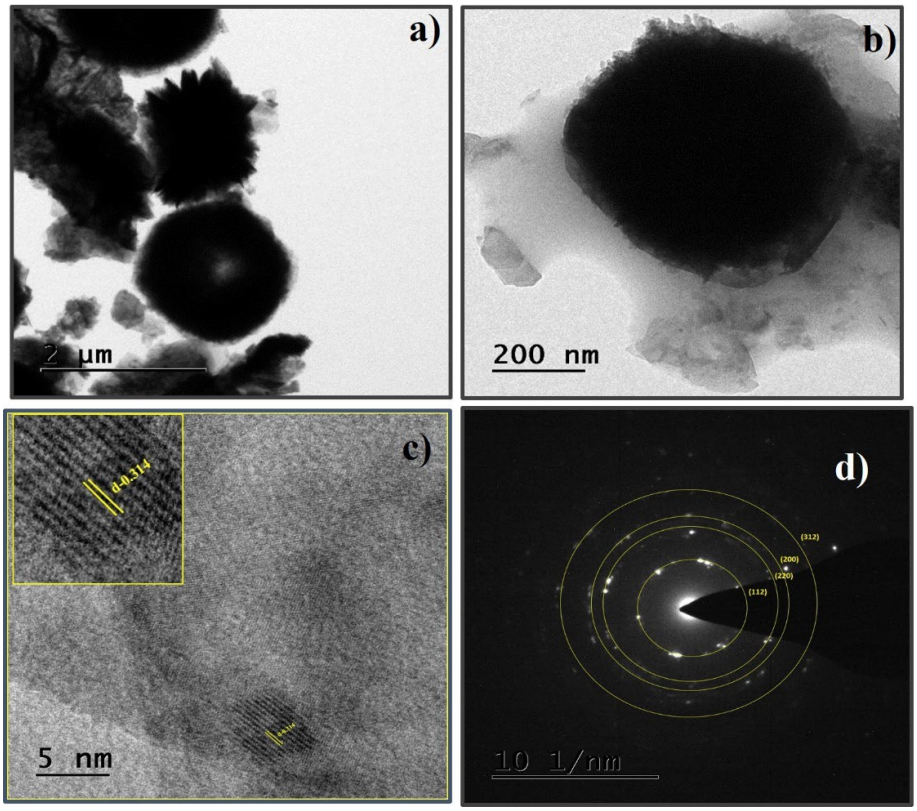

Figure 7. HR-TEM images of CZTS TU-10 nanostructures (a, b) images, (c) lattice pattern and d) SAED pattern

3.5. XPS analysis

The CZTS TU-10 sample was examined using X-ray photoelectron spectroscopy to determine its chemical composition and valance states. Figure 8a depicts the survey scan spectrum of the CZTS sample, which includes Cu, Zn, Sn, and S peaks. In addition, the impurity peaks noticed in the XPS spectrum, such as C and O, could be attributed to reference or pollution of the environment, whereas the impurity peak of N might be related to the remnants of the thiourea precursor [43].

High-resolution Cu 2p peaks were found at the binding energies of Cu $2p_{3/2}$ and Cu $2p_{1/2}$, which were 933.8 and 953.7 eV (Figure 8b), respectively, with a peak separation of 20.1 eV [44]. The observed results confirmed that the oxidation state of Cu was +2. For Zn, the peaks split into two energy states, Zn $2p_{3/2}$ and Zn $2p_{1/2,}$ were detected at 1021.9 and 1044.9 eV, respectively, with the distance between the two peaks at 23 eV (Figure 8c). The obtained results proved that Zn had an oxidation state of +2 [45]. The observed Sn peaks found at binding energies of 486.2 and 494.4 eV could be attributed to the Sn $3d_{5/2}$ and Sn $3d_{3/2}$ peaks (Figure 8d), which matched the conventional splitting of 8.2 eV [46]. The primary peak located at 164.8 eV and the small secondary peak detected at 171.2 eV (Figure 8e) could be assigned to the presence of S and S^{2-} [47]. The obtained valance states of Cu^{2+}, Zn^{2+}, $Sn^{4+,}$ and S^{2-} provide evidence that the prepared CZTS TU-10 sample was in good agreement with the stoichiometric formula of Cu_2ZnSnS_4.

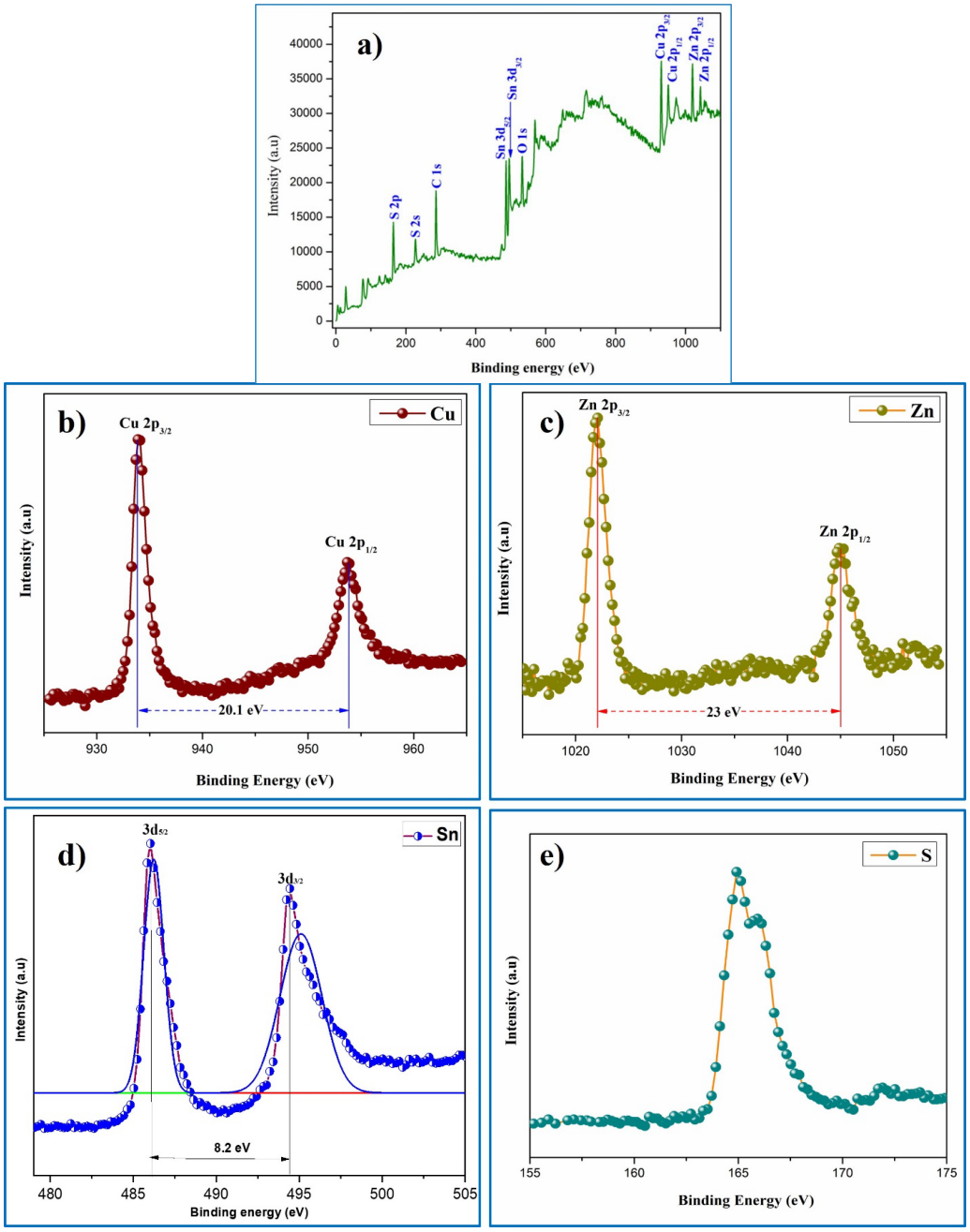

Figure 8. XPS spectra of CZTS TU-10 nanostructures (a) survey scan spectrum, (b) Cu, (c) Zn, (d) Sn, (e) S

3.6. Optical properties

The optical absorption characteristics of CZTS TU-10 were investigated using UV-Vis spectroscopy and evaluated in the 200-800 nm wavelength range. Figure 9a shows the absorption spectrum, which exhibited the characteristic absorption curve commonly observed in CZTS materials. Additionally, this absorption was related to CZTS TU-10 nanostructure refinement in forming crystals and large crystallite sizes. The presence of the absorption spectrum suggested that the CZTS TU-10 sample exhibited significant potential application in photocatalytic measurements [14]. The optical bandgap of CZTS TU-10 nanostructures for direct bandgap semiconductors was calculated using Tauc's plot [48],

$$\alpha h\nu = A(h\nu - E_g)^n \quad (8)$$

where hν is the photon energy, Eg is the optical bandgap of the products, A is a constant and n is 1/2 for direct bandgap semiconductors. The optical bandgap energy (Eg) of the CZTS sample was calculated by extrapolating the linear portion of $(\alpha h\nu)^2$ on the y-axis versus hν on the x-axis, as shown in Figure 9b. The calculated bandgap value of CZTS TU-10 nanostructures was 1.52 eV, which was consistent with that previously reported [49]. Furthermore, the obtained bandgap value could be attributed to the enhanced ordering within nanocrystals with a better crystalline nature.

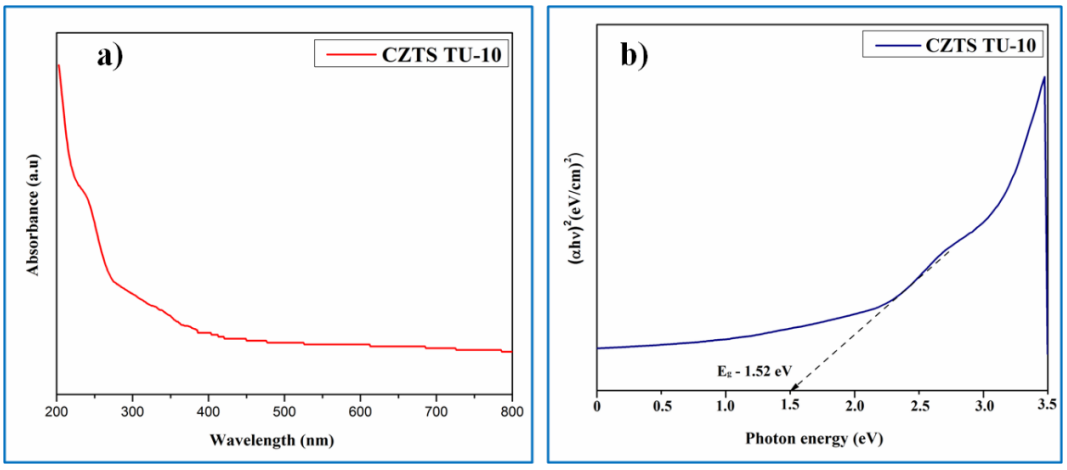

Figure 9. Optical properties of CZTS TU-10 nanostructures (a) UV-Vis absorbance, (b) Bandgap

3.7. Electrochemical measurement

3.7.1 Cyclic voltammetry

The electrochemical performance of the CZTS TU-10 sample was examined by cyclic voltammetry (CV), galvanostatic charge-discharge (GCD), and electron impendence spectroscopy (EIS) characterizations. CV study is a widely employed electrochemical approach utilized for the characterization of oxidation and reduction phenomena in molecular species, and investigations of electrochemical reactions facilitated by electron transfer mechanisms. Figure 10(a) displays the cyclic voltammetry (CV) curves obtained from the CZTS TU-10 electrode, within a potential range

of 0 to 0.6 V, while employing scanning rates ranging from 10 to 100 mV/s. The redox activity of the CZTS TU-10 electrode was confirmed by two redox peaks and shifted in higher positive (oxidation) and lower negative (reduction) potentials as the scan rate increased, which might be related to electric polarization and irreversible reactions [50]. Due to faster kinetics, the CV profiles demonstrated a steady voltammogram shape at increased scan rates, confirming that the electrode material had pseudo-capacitance behavior and better rate performance. Generally, the pseudo capacitors are capable of storing electrical charges through the process of surface redox reactions on the active substance, as well as the presence of OH^- ions inside the KOH solution. The specific capacitance (C_{sp}) of the CZTS TU-10 electrode was calculated using equation (2). Figure 10(b) shows the relationship between the specific capacitance (C_{sp}) vs. scan rate of the CZTS electrode and reveals that the C_{sp} values were increased as the scan rate was lowered from 100 to 10 mV/s. The calculated C_{sp} values were 389, 290, 232, 179, and 155 F/g for different scan rates of 10, 30, 50, 70, and 100 mV/s, respectively. The decrease in specific capacitance with increased scan rate was probably caused by the rapid redox reaction that occurred. Ionic diffusion only occurs in the outer region of surfaces when samples are scanned at higher scan rates, whereas at lower scan rates, both the inner and outer surfaces are involved in tuning the specific capacitance, which results in higher capacitance values [51]. Furthermore, the interplay between ions at the interface between the electrode and electrolyte is observed at higher scan rates, hence leading to decreased values of Csp.

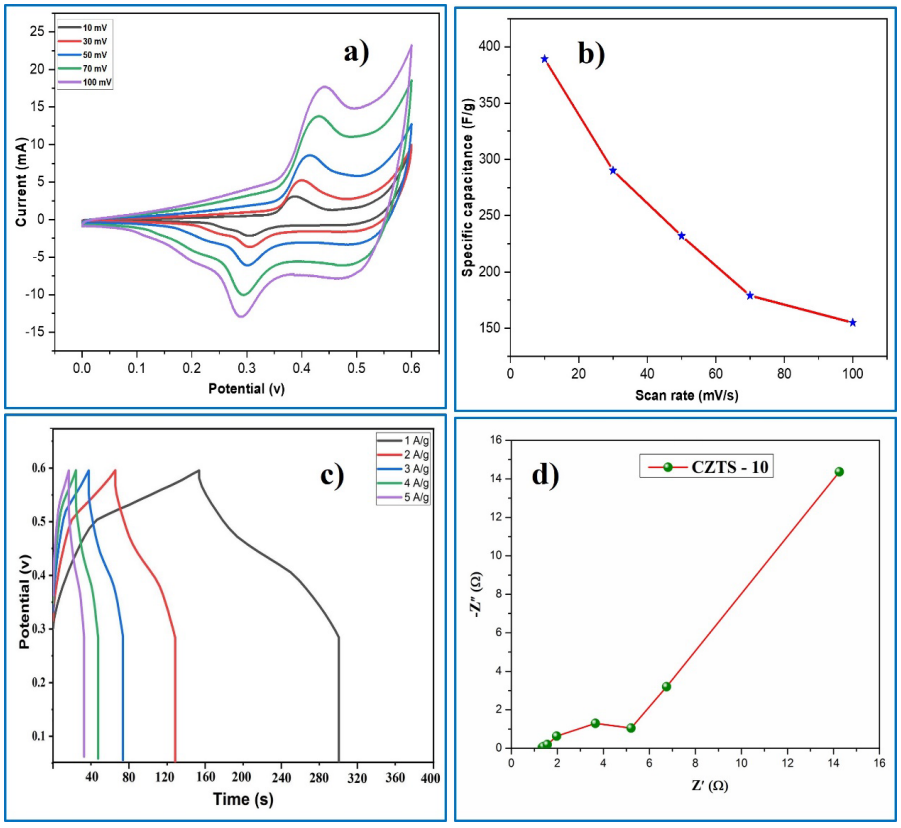

Figure 10. Electrochemical analysis of CZTS TU-10 nanostructures a) CV curve, b) scan rate vs specific capacitance, c) GCD curves, and d) EIS spectrum

3.7.2 Galvanostatic charge-discharge analysis

The specific capacitance of the fabricated electrode was determined by utilizing GCD charge-discharge measurements within the potential range of 0-0.6 V with various current densities (1-5 A/g), as shown in Figure 10(c). The nonlinear shape of the GCD profile with humps revealed faradic effects of the constructed electrode for different current density values. Equation (3) was used to calculate the Csp values, which were 368, 252, 216, 134, and 113 Fg^{-1} for the different current densities of 1, 2, 3, 4, and 5 Ag^{-1}, respectively. The obtained results indicate that the decreased Csp values were inversely proportional to increased current densities. This phenomenon could be ascribed to: (i) at high speeds, the electrode material could not react precisely; (ii) when the current density increased, the prepared electrode redox reaction was limited to the electrode outer surfaces, indicating a severe loss of capacitance; and (iii) as a result of the CZTS production method, an anhydrous surface was produced, which inhibited the transfer of cations, resulting in a rapid decrease in capacitance [52]. The surfactant-free CZTS TU-10 electrode had a high specific capacitance value of 368 Fg^{-1} at the current density of 1 Ag^{-1} due to the better electrochemical performance with an optimal crystallite size, narrow bandgap, and also due to the distinct flower-like morphology. The results discussed above clearly indicate that the sulfur-rich, surfactant-free CZTS TU-10 electrode material exhibited superior performance when utilized in energy storage applications.

3.7.3 EIS spectroscopy

The CZTS TU-10 electrode was subjected to electrochemical impedance spectroscopy to examine the fundamental characteristics of the electrode and electrolyte interfaces where charge reactions and ion transfer occurred in the system. The Nyquist plot and associated equivalent circuit are displayed in Figure 10(d). The phenomenon of a semicircle transitioning into a straight line was noticed at higher frequencies, whereas at lower frequencies, the semicircle transformed into a linear shape. The presence of small semicircle frequencies could be attributed to the charge transfer resistance occurring at the interface of the active material [53].

3.8. Photocatalytic activity of CZTS nanostructures

3.8.1 Photocatalytic mechanism

The absorption spectra of the degradation of MB and CV dye solutions under sunlight in the presence of CZTS as a catalyst are shown in Figure 11(a, b). The spectra revealed that the maximum absorbance wavelengths of the CV and MB dyes were centered at 570 nm and 664 nm, respectively. The results demonstrated that the absorbance of the solutions decreased with increasing time interval, indicating that the dye concentrations decreased as the exposure time increased [54, 55]. As shown in Figure 11a, the CZTS nanostructures using MB dye had a higher degradation efficiency compared to CV dye after 70 min. It is well known that large surface area, morphology, crystallinity, and particle size of a material are crucial to its photocatalytic activity. Consequently, morphology may play a significant role in calculating the final degradation efficiency. In the present work, the flower-like CZTS TU-10 sample had a high removal efficiency due to the high surface area and smaller particle size of the CZTS catalyst. The results also suggested that a suitable preparation method could be used to enhance photocatalytic performance.

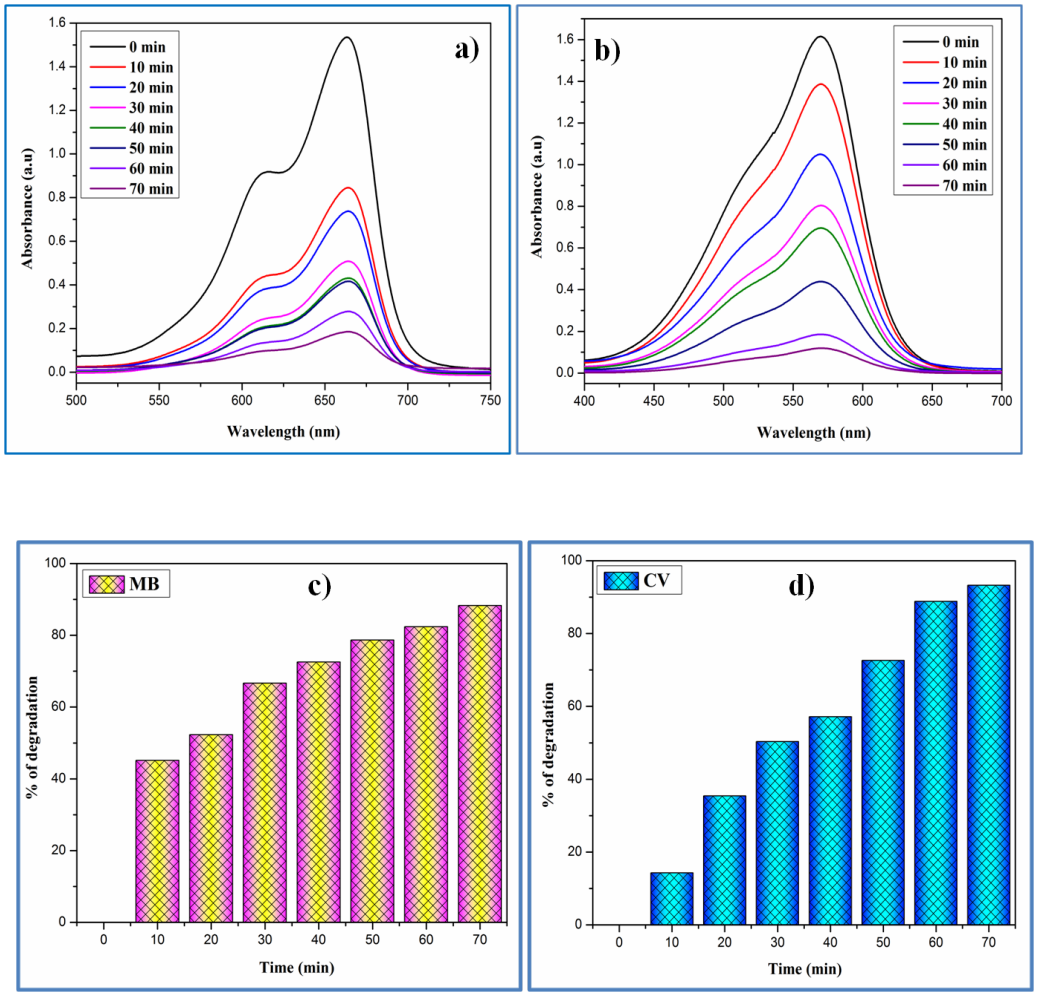

Figure 11. Absorbance vs wavelength spectra of CZTS TU-10 catalyst (a) methylene blue (b) crystal violet dyes. Degradation efficiency of CZTS TU-10 (c) MB, (d) CV dyes

3.8.2 Degradation efficiency

The degradation efficiencies of CZTS TU-10 nanostructures were investigated, and the results are shown in Figure 11(c, d). The experimental results clearly revealed that the flower-like CZTS TU-10 photocatalyst had the highest degradation efficiency of 89% against MB and 93% efficiency against CV dye in 70 min. As a result, the surfactant-free CZTS nanoparticles produced by the hydrothermal process served as an efficient photocatalyst for the degradation of toxic dyes. In a photocatalytic system, a photoinduced molecular transformation occurs on the surface of the photocatalyst. Electrons jump from the valance band to the conduction band when the surface of a photocatalytic material is exposed to an energy equal to or greater than the bandgap. This causes a negatively charged electron to appear in the conduction band and a positively charged hole to appear in the valance band. The conduction band electron reduces the adsorbed oxygen onto the photocatalytic surface, and the positively charged hole oxidizes the organic contaminants into

hydroxyl free radicals. The probable mechanism of dye degradation in the presence of CZTS, which acts as a catalyst when exposed to sunlight, was described in detail in our previous study [56]. Table 3 compares previously reported data of CZTS prepared by various synthesis processes, as well as their morphologies, efficiencies, bandgaps, degradation rates, type of dyes, and time needed for complete degradation of dyes. The results revealed that the prepared CZTS TU-10 nanostructures had higher degradation rates of CV and MB dye, which were attributed to the presence of small crystallite size, narrow band-gap (1.52 eV), and a rose flower-like morphology.

Table 3. Comparison of degradation efficiency of CZTS catalyst with various preparation methods

Catalyst	Method	Morphology	Bandgap (eV)	Dye	Degradation Efficiency	Time (min)	Ref
Cu_2ZnSnS_4	Microwave	Spherical	-	MB	30%	240	[57]
Cu_2ZnSnS_4	Hydrothermal	Agglomerated nanoparticles	1.53	MB	50%	45	[14]
Cu_2ZnSnS_4	Hydrothermal	Spherical	1.51	RhB	55%	240	[58]
Cu_2ZnSnS_4	Hydrothermal	Flower-like with nanosheets	1.53	MB	60%	90	[59]
Wurtzite CZTS	Hot-injection	Nano-Spheres	1.54	Organic pollutants and textile waste	73%	150	[60]
Wurtzite CZTS	Hot-injection	Nano-rods	1.51	Organic pollutants and textile waste	90.3%	160	[61]
Kesterite CZTS	One-pot	Nanocrystals	1.51	MO	91%	60	[62]
Cu_2ZnSnS_4	Hydrothermal	Rose-flower like	1.52	MB	89	70	Present work
Cu_2ZnSnS_4	Hydrothermal	Rose-flower like	1.52	CV	93	70	Present work

3.9 Antibacterial activity

The antibacterial activity of Au, Ag, ZnO, and TiO_2 nanoparticles against gram-positive and gram-negative bacterial strains has gained particular attention in recent years; however, no such notable antimicrobial study has been conducted on CZTS nanoparticles to date. It is known that inorganic nanomaterials contain minerals essential to human health. These minerals exhibit notable activity at low concentrations and are less hazardous more stable, and more heat resistant [63-65]. Another important parameter for antibacterial agents is that these nanoparticles should not be toxic to human

cells *in vivo*. In this regard, CZTS nanoparticles offer the advantages of low toxicity and significant antibacterial activity at low concentrations, all of which are needed for these nanomaterials to act as potent antimicrobial agents inside most living systems. Several previous studies involving a variety of inorganic materials containing Zn, Cu, Sn, S, etc., elements reported very high responsiveness toward pathogenic microorganisms with minimal effects on human cell lines and indicating that these inorganic materials possessed significant antibacterial properties. The potential benefits of CZTS nanoparticles in terms of antimicrobial activity against a variety of significant pathogenic strains generated significant interest in their effective and applicability [66].

In the present work, the antibacterial activity of synthesized CZTS TU-10 nanostructures was carried out against both gram-positive (*Streptococcus pneumoniae, Streptococcus pyogenes*) and gram-negative (*Klebsiella pneumoniae, Vibrio parahaemolyticus*) pathogens. Figure 12(a-d) shows the results of the investigation of the antibacterial properties of CZTS nanostructures evaluated by the zone of inhibition (ZOI). Remarkably, following 24 h of incubation, the synthesized CZTS nanostructures exhibited an inhibition zone around them for all the bacterial strains tested. This observation served as an indication of the bacteriostatic capability of the CZTS nanostructures. Additionally, the size of the inhibition zone varied depending on the specific type of bacteria. The observed suppression of bacterial growth could be related to detrimental effects on the bacterial cell membrane and the resultant expulsion of cytoplasmic contents, ultimately leading to the bacterium's death. The zone of inhibition diameter was calculated to correspond to pathogens, and the values are listed in Table 4, which reveals that the inhibition growth increased with increasing concentration of CZTS. The maximum inhibition zone was obtained against *V. parahaemolyticus* bacteria at 18, 20, 22, and 26 mm, corresponding to 25, 50, 75, and 100 µg/mL, respectively. The change in the inhibition zone depended on the type of bacteria, particle size, and concentration of nanoparticles. To date, some mechanisms have been suggested for the antibacterial properties exhibited by inorganic nanoparticles: (i) The release of metal cations from nanoparticles leads to interactions with proteins, nucleic acids, and microbial membranes, resulting in structural modifications and inhibition of microbial replication; (ii) The internalization of nanoparticles through ion channels or proteins at the cell wall results in the mechanical breakdown of the cell membrane; (iii) The nanoparticle surface generates reactive oxygen species (ROS), including hydroxyl radicals (OH), hydrogen peroxide (H_2O_2), and superoxide ($^{\cdot}O_2^-$). These ROS can potentially cause significant damage to lipids, DNA, and proteins within the cell membrane, resulting in leakage and degradation of the bacterial cell membrane [67, 68]. Based on this investigation, hydrothermally prepared CZTS TU-10 nanostructures had strong antibacterial performance against *V. parahaemolyticus* bacteria due to their superior morphology, large surface area, and small particle size.

4. Conclusions

The pure kesterite phase of CZTS nanostructures was successfully synthesized using a low-cost hydrothermal method without the assistance of surfactants or capping agents. XRD and Raman studies confirmed the growth of pure-phase CZTS nanostructures that had been synthesized with varying initial sulfur concentrations. FESEM studies indicate that different sulfur sources had a strong influence on the morphological changes of CZTS. The interplanar distance value was calculated from the HRTEM image and found to be 0.31 nm, which strongly supported the XRD result. The valance states of CZTS were confirmed by XPS. Surfactant-free pure kesterite CZTS TU-10 was found to be a good photocatalyst for MB and CV dyes with degradation efficiencies of 89% and 93% within 70 min. The prepared CZTS TU-10 electrode offered an excellent specific

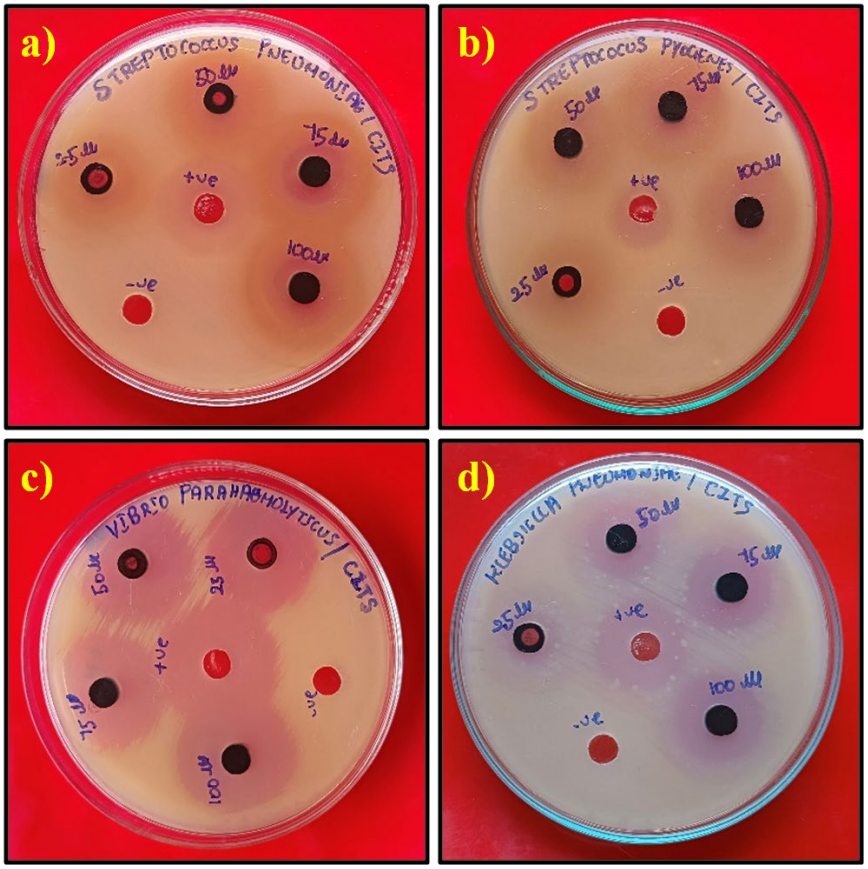

Figure 12. Antibacterial activity of the CZTS TU-10 nanostructures (a) *Streptococcus pneumoniae*, (b) *Streptococcus pyogenes*, (c) *Klebsiella pneumoniae*, (d) *Vibrio parahaemolyticus*

Table 4. Antibacterial activity of CZTS TU-10 nanostructures

S.No	Test Organisms	Zone of Inhibition (mm)					
		25 µL	50 µL	75 µL	100 µL	Positive Control	Negative Control
1.	*Streptococcus pneumoniae*	12 mm	14 mm	16 mm	20 mm	26 mm	-
2.	*Streptococcus pyogenes*	14 mm	16 mm	18 mm	21 mm	26 mm	-
3.	*Klebsiella pneumoniae*	12 mm	14 mm	16 mm	18 mm	26 mm	-
4.	*Vibrio parahaemolyticus*	18 mm	20 mm	22 mm	26 mm	29 mm	-

capacitance of 389 Fg^{-1} at 10 mV/s by CV measurements. Finally, the surfactant-free CZTS TU-10 sample possessed a flower-like morphology and showed excellent degradation efficiency, superior antibacterial activity, and high specific capacitance, all of which revealed that prepared CZTS nanostructures could be potential candidates for future applications.

5. Acknowledgements

The corresponding author wishes to thank the Head of the Department of Physics and Centralized Instrumentation and Service Laboratory (CISL), Annamalai University, Annamalai Nagar, Tamil Nādu, India, for providing the CV and analytical instrument facilities.

References

[1] Jabeen, U., Shah, S.M., Aamir, M. and Ahmad, I., 2021. Grafting and co-grafting of dyes on Cd-doped ZnS nanocrystals and their application on dye-sensitized solar cells. *Bulletin of Materials Science*, 44, https://doi.org/10.1007/s12034-021-02575-3.

[2] Zainol, N., Aziz, N.H., Jazlan, C.A.I.C. and Razahazizi, N.A., 2023. The application of design of experiments in the hatchery wastewater treatment through biological method. *Current Applied Science and Technology*, 23(2), https://doi.org/10.55003/cast.2022.02.23.003.

[3] Bhat, K.S. and Nagaraja, H.S., 2019. Morphology-dependent electrochemical performances of nickel hydroxide nanostructures. *Bulletin of Materials Science*, 42(6), https://doi.org/10.1007/s12034-019-1951-9.

[4] Reddy, B.J., Vickraman, P. and Justin, A.S., 2019. A facile synthesis of novel α-$ZnMoO_4$ microspheres as electrode material for supercapacitor applications. *Bulletin of Materials Science*, 42(2), https://doi.org/10.1007/s12034-019-1749-9.

[5] Samiei, E., Mohammadi, S., Torkzadeh-Mahani, M. and Askari, M.B., 2021. Preparation and characterization of $ZnCo_2O_4$ as a binary transitional metal oxide towards pseudocapacitor electrode materials. *Brazilian Journal of Physics*, 51, 420-428.

[6] Devaraj, S. and Munichandraiah, N., 2008. Effect of crystallographic structure of MnO_2 on its electrochemical capacitance properties. *The Journal of Physical Chemistry C*, 112(11), 4406-4417.

[7] Zhang, L.L. and Zhao, X.S., 2009. Carbon-based materials as supercapacitor electrodes. *Chemical Society Reviews*, 38(9), 2520-2531.

[8] Iqbal, M.W., Faisal, M.M., Hassan, H., Afzal, A.M., Aftab, S., Zahid, T. and Rehman, A., 2022. Facile hydrothermal synthesis of high-performance binary silver-cobalt-sulfide for supercapattery devices. *Journal of Energy Storage*, 52, https://doi.org/10.1016/j.est.2022.104847.

[9] Tarish, S., Xu, Y., Wang, Z., Mate, F., Al-Haddad, A., Wang, W. and Lei, Y., 2017. Highly efficient biosensors by using well-ordered ZnO/ZnS core/shell nanotube arrays. *Nanotechnology*, 28(40), https://doi/org/10.1088/1361-6528/aa82b0.

[10] Li, B., Zheng, M., Xue, H. and Pang, H., 2016. High performance electrochemical capacitor materials focusing on nickel based materials. *Inorganic Chemistry Frontiers*, 3(2), 175-202.

[11] Sarkar, S., Das, B., Midya, P.R., Das, G.C. and Chattopadhyay, K.K., 2015. Optical and thermoelectric properties of chalcogenide based Cu_2NiSnS_4 nanoparticles synthesized by a novel hydrothermal route. *Materials Letters*, 152, 155-158.

[12] Gurav, K.V., Pawar, S.M., Shin, S.W., Surayawanshi, M.P., Agawane, G.L., Patil, P.S., Moon, J.H., Yun, J.H. and Kim, J.H., 2013. Electrosynthesis of CZTS films by sulfurization of CZT

precursor: Effect of soft annealing treatment. *Applied Surface Science*, 283, 74-80.

[13] Norris, D.J., Yao, N., Charnock, F.T. and Kennedy, T.A., 2001. High-quality manganese-doped ZnSe nanocrystals. *Nano Letters*, 1(1), 3-7.

[14] Phaltane, S.A., Vanalakar, S.A., Bhat, T.S., Patil, P.S., Sartale, S.D. and Kadam, L.D., 2017. Photocatalytic degradation of methylene blue by hydrothermally synthesized CZTS nanoparticles. *Journal of Materials Science: Materials in Electronics*, 28, 8186-8191.

[15] Gurav, K.V., Yun, J.H., Pawar, S.M., Shin, S.W., Suryawanshi, M.P., Kim, Y.K., Agawane, G.L., Patil, P.S. and Kim, J.H., 2013. Pulsed electrodeposited CZTS thin films: Effect of duty cycle. *Materials Letters*, 108, 316-319.

[16] Zaberca, O., Oftinger, F., Chane-Ching, J.Y., Datas, L., Lafond, A., Puech, P., Balocchi, A., Lagarde, D. and Marie, X., 2012. Surfactant-free CZTS nanoparticles as building blocks for low-cost solar cell absorbers. *Nanotechnology*, 23(18), https://doi.org/10.1088/0957-4484/23/18/185402.

[17] Patil, U., Dhanasekar, M., Kadrekar, R., Arya, A., Bhat, S.V. and Late, D.J., 2022. Efficient humidity sensor based on surfactant free Cu_2ZnSnS_4 nanoparticles. *Ceramics International*, 48(19), 28898- 28905.

[18] Yu, X., Shavel, A., An, X., Luo, Z., Ibáñez, M. and Cabot, A., 2014. Cu_2ZnSnS_4-Pt and Cu_2ZnSnS_4-Au heterostructured nanoparticles for photocatalytic water splitting and pollutant degradation. *Journal of the American Chemical Society*, 136(26), 9236-9239, https://doi.org/10.1021/ja502076b.

[19] Quinson, J., 2021. Surfactant-free precious metal colloidal nanoparticles for catalysis. *Frontiers in Nanotechnology*, 3, https://doi.org/10.3389/fnano.2021.770281.

[20] Choudhary, S., Sahu, K., Bisht, A., Singhal, R. and Mohapatra, S., 2020. Template-free and surfactant-free synthesis of CeO_2 nanodiscs with enhanced photocatalytic activity. *Applied Surface Science*, 503, https://doi.org/10.1016/j.apsusc.2019.144102.

[21] Harinipriya, S., Cassian, H. and Sudha, V., 2021. Colloidal CCTS nanoparticle synthesis by solution method for solar photovoltaic applications. *Journal of Materials Research and Technology*, 15, 3558- 3569.

[22] Zaman, M.B., Mir, R.A. and Poolla, R., 2019. Growth and properties of solvothermally derived highly crystalline Cu_2ZnSnS_4 nanoparticles for photocatalytic and electrocatalytic applications. *International Journal of Hydrogen Energy*, 44(41), 23023-23033.

[23] Chaudhari, V.P., Roy, S.M., Chaudhuri, T.K. and Roy, D.R., 2022. Synthesis, characterization and significant antimicrobial properties of CZTS nanoparticles against pathogenic strains. *Journal of the Indian Chemical Society*, 99(3), https://doi.org/10.1016/j.jics.2022.100351.

[24] Robati, S.M., Imani, M. and Tadjarodi, A., 2018. Ultrafast synthesis of crystalline Cu_2ZnSnS_4 nanoparticles by solid state microwave heating technique and study of their electrochemical behavior. *Materials Letters*, 225, 9-12.

[25] Paraye, A., Ramachandran, M. and Selvam, N.V., 2021. Facile ultrasound-assisted synthesis of copper zinc tin sulfide chalcogenide nanoparticles for thin film solar cell applications. *Periodica Polytechnica Chemical Engineering*, 65(1), 42-49.

[26] Shi, B., Liu, W., Zhu, K. and Xie, J., 2017. Synthesis of flower-like copper sulfides microspheres as electrode materials for sodium secondary batteries. *Chemical Physics Letters*, 677, 70-74.

[27] Rawat, K. and Shishodia, P.K., 2017. Structural and optical properties of sol-gel derived Cu_2ZnSnS_4 nanoparticles, *Advanced Powder Technology* 28(2), 611-617.

[28] Long, B., Cheng, S., Ye, D., Yue, C. and Liao, J., 2019. Mechanistic aspects of preheating effects of precursors on characteristics of Cu_2ZnSnS_4 (CZTS) thin films and solar cells. *Materials Research Bulletin*, 115, 182-190.

[29] Liqiang, J., Yichun, Q., Baiqi, W., Shudan, L., Baojiang, J., Libin, Y., Wei, F., Honggang, F. and Jiazhong, S., 2006, Review of photoluminescence performance of nano-sized

semiconductor materials and its relationships with photocatalytic activity. *Solar Energy Materials and Solar Cells*, 90(12), 773-787.

[30] Yang, Y., Ding, Y., Zhang, J., Liang, N., Long, L. and Liu, J., 2022. Insight into the growth mechanism of mixed phase CZTS and the photocatalytic Performance. *Nanomaterials*, 12(9), https://doi.org/10.3390/nano12091439.

[31] Waluś, E., Manecki, M., Cios, G. and Tokarski, T., 2021. Effect of a sulfur precursor on the hydrothermal synthesis of Cu_2MnSnS_4. *Materials*, 14(13), https://doi.org/10.3390/ma14133457.

[32] Rovelli, L., Tilley, S.D. and Sivula, K., 2013. Optimization and stabilization of electrodeposited Cu_2ZnSnS_4 photocathodes for solar water reduction. *ACS Applied Materials and Interfaces*, 5(16), 8018-8024.

[33] Verma, S.K., Agrawal, V., Jain, K., Pasricha, R. and Chand, S., 2013, Green synthesis of nanocrystalline Cu_2ZnSnS_4 powder using the hydrothermal route. *Journal of Nanoparticles*, 2013, https://doi.org/10.1155/2013/685836.

[34] Bahramzadeh, S., Abdizadeh, H. and Golobostanfard, M.R., 2015. Controlling the morphology and properties of solvothermal synthesized Cu_2ZnSnS_4 nanoparticles by solvent type. *Journal of Alloys and Compounds*, 642, 124-130.

[35] Winkler, M.T., Wang, W., Gunawan, O., Hovel, H.J., Todorov, T.K. and Mitzi, D.B., 2014. Optical designs that improve the efficiency of $Cu_2ZnSn(S,Se)_4$ solar cells. *Energy and Environmental Science*, 7(3), 1029-1036.

[36] Shafi, M.A., Khan, L., Ullah, S., Bouich, A., Ullah, H. and Mari, B., 2022. Synthesis of CZTS kesterite by pH adjustment in order to improve the performance of CZTS thin film for photovoltaic applications. *Micro and Nanostructures*, 164, https://doi.org/10.1016/j.spmi.2022.107185.

[37] Shalabayev, Z., Baláz, M., Daneu, N., Dutková, E., Bujňáková, Z., Kaňuchová, M., Danková, Z., Balážová, L., Urakaev, F., Tkáčiková, L. and Burkitbayev, M., 2019. Sulfur-mediated mechanochemical synthesis of spherical and needle-like copper sulfide nanocrystals with antibacterial activity. *ACS Sustainable Chemistry and Engineering*, 7(15), 12897-12909.

[38] Guo, Y., Wei, J., Yang, T., Lv, Z. and Xu, Z., 2019. Manipulation of surface plasmon resonance for high photocatalytic activity of Ag-Bi2WO6 hetero-architecture. *Optik*, 180, 285-294.

[39] Lixiong, Y., Dan, W., Jianfeng, H., Liyun, C., Haibo, O., Jianpeng, W. and Xiang, Y., 2015. Microwave hydrothermal synthesis and photocatalytic activities of morphology-controlled ZnS crystallites. *Ceramics International*, 41(2), 3288-3292.

[40] Singh, O.P., Parmar, R., Gour, K.S., Dalai, M.K., Tawale, J., Singh, S.P. and Singh, V.N., 2015. Synthesis and characterization of petal type CZTS by stacked layer reactive sputtering. *Superlattices and Microstructures*, 88, 281-286.

[41] Ghosh, A., Biswas, A., Thangavel, R. and Udayabhanu, G., 2016. Photo-electrochemical properties and electronic band structure of kesterite copper chalcogenide Cu 2–II–Sn–S 4 (II= Fe, Co, Ni) thin films. *RSC Advances*, 6(98), 96025-96034.

[42] Keller, A.A., Vosti, W., Wang, H. and Lazareva, A., 2014. Release of engineered nanomaterials from personal care products throughout their life cycle. *Journal of Nanoparticle Research*, 16, 1-10.

[43] Henríquez, R., Nogales, P.S., Moreno, P.G., Cartagena, E.M., Bongiorno, P.L., Navarrete-Astorga, E. and Dalchiele, E.A., 2023. One-step hydrothermal synthesis of Cu_2ZnSnS_4 nanoparticles as an efficient visible light photocatalyst for the degradation of congo red azo dye. *Nanomaterials*, 13(11), https://doi.org/10.3390/nano13111731.

[44] Patil, S.S., Mane, R.M., Mali, S.S., Hong, C.K. and Bhosale, P.N., 2020. Facile designing and assessment of photovoltaic performance of hydrothermally grown kesterite Cu_2ZnSnS_4 thin films: influence of deposition time. *Solar Energy*, 201, 102-115.

[45] Zaman, M.B., Mir, R.A. and Poolla, R., 2019. Growth and properties of solvothermally derived highly crystalline Cu_2ZnSnS_4 nanoparticles for photocatalytic and electrocatalytic

applications. *International Journal of Hydrogen Energy*, 44(41), 23023-23033.
[46] Mkawi, E.M., Al-Hadeethi, Y., Al-Hartomy, O. and Bekyarova, E., 2020. Size-controlling of Cu_2ZnSnS_4 nanoparticles: Effects of stabilizing/reducing agents on material properties. *Results in Physics*, 19, https://doi.org/10.1016/j.rinp.2020.103407.
[47] Mirbagheri, N., Engberg, S., Crovetto, A., Simonsen, S.B., Hansen, O., Lam, Y.M. and Schou, J., 2016. Synthesis of ligand-free CZTS nanoparticles via a facile hot injection route. *Nanotechnology*, 27(18), https://doi.org/10.1088/0957-4484/27/18/185603.
[48] Khammar, M., Ynineb, F., Guitouni, S., Bouznit, Y. and Attaf, N., 2020. Crystallite size and intrinsic strain contribution in band gap energy redshift of ultrasonic-sprayed kesterite CZTS nanostructured thin films. *Applied Physics A*, 126(6), https://doi.org/10.1007/s00339-020-03591-6.
[49] Rajesh, G., Muthukumarasamy, N., Subramanian, E.P., Venkatraman, M.R., Agilan, S., Ragavendran, V., Thambidurai, M., Velumani, S., Yi, J. and Velauthapillai, D., 2015. Solution-based synthesis of high yield CZTS (Cu_2ZnSnS_4) spherical quantum dots. *Superlattices and Microstructures*, 77, 305-312.
[50] Zhao, Y., Yan, J., Huang, Y., Lian, J., Qiu, J., Bao, J., Cheng, M., Xu, H., Li, H. and Chen, K., 2018. Interfacial self-assembly of monolayer Mg-doped NiO honeycomb structured thin film with enhanced performance for gas sensing. *Journal of Materials Science: Materials in Electronics*, 29, 11498-11508.
[51] Premkumar, V.K., Sivakumar, G., Dinesh, S. and Barathan, S., 2017. Facile hydrothermal synthesis of cobalt stannate (Co_2SnO_4) nano particles for electrochemical properties. *Journal of Materials Science: Materials in Electronics*, 28, 4780-4787.
[52] Farzi, M., Moradi, M., Hajati, S., Toth, J. and Kazemzadeh, A., 2021. Synthesis of rod-like ternary Cu (Cd)-In-S and quaternary Cu-Cd-In-S by controlled ion exchange of MIL-68 (In) derived indium sulfide for high energy-storage capacitor. *Synthetic Metals*, 278, https://doi.org/10.1016/j.synthmet.2021.116815.
[53] Sarkar, S., Howli, P., Das, B., Das, N.S., Samanta, M., Das, G.C. and Chattopadhyay, K.K., 2017. Novel quaternary chalcogenide/reduced graphene oxide-based asymmetric supercapacitor with high energy density. *ACS Applied Materials and Interfaces*, 9(27), 22652-22664.
[54] Fan, J., Li, T. and Heng, H., 2016. Hydrothermal growth of ZnO nanoflowers and their photocatalyst application. *Bulletin of Materials Science*, 39, 19-26.
[55] Zhou, Z., Zhang, P., Lin, Y., Ashalley, E., Ji, H., Wu, J., Li, H. and Wang, Z., 2014. Microwave fabrication of Cu_2ZnSnS_4 nanoparticle and its visible light photocatalytic properties. *Nanoscale Research Letters*, 9, https://doi.org/10.1186/1556-276X-9-477.
[56] Manjula, S., Sarathkumar, A. and Sivakumar, G., 2023. Hydrothermally synthesized Cu_2ZnSnS_4 nanoparticles for photocatalytic degradation of Rhodamine B dye. *Journal of Nano Research*, 79, 25-36.
[57] Sawant, J.P., Rajput, R., Patil, S., Ryu, J., Patil, D.R. and Kale, R.B., 2021. Photocatalytic activities of hydrothermal synthesized copper zinc tin sulfide nanostructures. *Journal of Materials Science: Materials in Electronics*, 32, 22803-22812.
[58] Sheebha, I., Venugopal, V., James, J., Maheskumar, V., Sakunthala, A. and Vidhya, B., 2020. Comparative studies on hierarchical flower like Cu2XSnS4 [X= Zn, Ni, Mn & Co] quaternary semiconductor for electrocatalytic and photocatalytic applications. *International Journal of Hydrogen Energy*, 45(15), 8139-8150.
[59] Semalti, P., Sharma, V. and Sharma, S.N., 2021. A novel method of water remediation of organic pollutants and industrial wastes by solution-route processed CZTS nanocrystals. *Journal of Materiomics*, 7(5), 904-919.
[60] Hou, X., Li, Y., Yan, J.J. and Wang, C.W., 2014. Highly efficient photocatalysis of p-type Cu_2ZnSnS_4 under visible-light illumination. *Materials Research Bulletin*, 60, 628-633.
[61] Kumar, R.S., Maddirevula, S., Easwaran, M., Dananjaya, S.H.S. and Kim, M.D., 2015.

Antibacterial activity of novel Cu_2ZnSnS_4 nanoparticles against pathogenic strains. *RSC Advances*, 5(129), 106400-106405.

[62] Khashan, K.S., Sulaiman, G.M., Ameer, F.A.K.A. and Napolitano, G., 2016. Synthesis, characterization and antibacterial activity of colloidal NiO nanoparticles. *Pakistan Journal of Pharmaceutical Sciences*, 29(2), 541-546.

[63] Chaudhari, V.P., Roy, S.M., Chaudhuri, T.K. and Roy, D.R., 2022. Synthesis, characterization and significant antimicrobial properties of CZTS nanoparticles against pathogenic strains. *Journal of the Indian Chemical Society*, 99(3), https://doi.org/10.1016/j.jics.2022.100351.

[64] Chaudhari, V.P., Rajput, K., Roy, S.M., Chaudhuri, T.K. and Roy, D.R., 2022. Experimental and first- principles investigation on the structural, electronic and antimicrobial properties of nickel hydroxide nanoparticles. *Journal of Physics and Chemistry of Solids*, 160, https://doi.org/10.1016/j.jpcs.2021.110367.

[65] Verma, A., Uzun, O., Hu, Y., Hu, Y., Han, H.S., Watson, N., Chen, S., Irvine, D.J. and Stellacci, F., 2008. Surface-structure-regulated cell-membrane penetration by monolayer-protected nanoparticles. *Nature Materials*, 7(7), 588-595.

[66] Nel, A.E., Mädler, L., Velegol, D., Xia, T., Hoek, E.M., Somasundaran, P., Klaessig, F., Castranova, V. and Thompson, M., 2009. Understanding bio physico chemical interactions at the nano-bio interface. *Nature Materials*, 8(7), 543-557.

[67] Yılmaz, G.E, Göktürk, I., Ovezova, M., Yılmaz, F., Kılıç, S. and Denizli, A., 2023. Antimicrobial nanomaterials: a review. *Hygiene*, 3(3), 269-290.

[68] Franco, D., Calabrese G., Guglielmino, S.P.P. and Conoci, S., 2022. Metal-based nanoparticles: Antibacterial mechanisms and biomedical application. *Microorganisms*, 10(9), https://doi.org/10.3390/microorganisms10091778.